

## Research Article

# Physicochemical Characterization and Biocompatibility of SPION@Plasmonic @Chitosan Core-Shell Nanocomposite Biosynthesized from Fungus Species

M. M. Eid <sup>1</sup>, S. M. El-Hallouty,<sup>2</sup> M. El-Manawaty,<sup>2</sup> and F. H. Abdelzaher<sup>3</sup>

<sup>1</sup>Spectroscopy Department, National Research Centre, Dokki, Giza, Egypt

<sup>2</sup>Pharmacognosy Department, National Research Centre, Dokki, Giza, Egypt

<sup>3</sup>Microbiology Department, National Research Centre, Dokki, Giza, Egypt

Correspondence should be addressed to M. M. Eid; maybaker25@gmail.com

Received 23 May 2018; Revised 27 August 2018; Accepted 4 November 2018; Published 5 February 2019

Guest Editor: Alex López Córdoba

Copyright © 2019 M. M. Eid et al. This is an open access article distributed under the Creative Commons Attribution License, which permits unrestricted use, distribution, and reproduction in any medium, provided the original work is properly cited.

In this work we aim to manipulate green route for the synthesis of core-shell maghemite-based Ag nanoparticles functionalized with chitosan. Three fungal species, *Aspergillus deflexus*, *Fusarium oxysporum*, and *Penicillium pinophilum*, were used in the process of synthesis to select the best among them for the production. The physicochemical parameters of produced nanoparticles and mediated cytotoxicity assessment for their potential medical application have been performed using Fourier transform infrared (FTIR), UV/visible, vibrating sample magnetometer (VSM), dynamic light scattering (DLS), high-resolution transmission electron microscope (HRTEM), EDAX, and MTT to plot a cytotoxicity assessment report. The results confirmed the formation of monodispersed  $\gamma\text{Fe}_2\text{O}_3$ @Ag@chitosan with low cytotoxicity against prostate (PC3), liver (HepG2), column (HCT116), and breast cancer (MCF7) ATCC cell lines. In conclusion, these results prove the success of the green route used for the biosynthesis of  $\gamma\text{Fe}_2\text{O}_3$ @Ag@chitosan with parameters necessary for bioimaging, drug and gene delivery, and biosensing.

## 1. Introduction

The nanoscience is the study of the properties of matter at the nanoscale [1]. Taniguchi was the first [2] to define the word “nanotechnology” as to consist of the processes of separation, consolidation, and deformation of materials by one atom or one molecule. Since then, the interest of application of nanotechnology is growing in the industry, medicine, electronics, and environment [3].

Numerous methods have been employed to synthesize nanomaterial with controlled size and shape. These methods are generally classified into top-down and bottom-up. The green chemistry is an alternative low cost, an ecofriendly route that has increasingly applied for the nanoparticle synthesis. Plants, algae, bacteria, fungus, yeast, and human cells were extensively subjected to studies recently to select best candidates for the efficient synthesis. These biosystems contribute to the synthesis by the reduction of metal ions into metal atoms

and the stabilization of the produced nanoparticles by working as capping agents. Biosynthesis as a growing field is intended to displace environmentally and energy unfavorable toxic materials derived from petrochemicals [4–6].

The super paramagnetic nanoparticles are one of the highly interesting metals owing to their fantastic properties that have been manipulated in a wide range of applications. In medicine, the ease of separation, the biocompatibility, the high surface to volume ratio, and the high refractive index permit their use in efficient drug targeting, MRI, enhanced SPR biosensors, and hyperthermia cancer therapy [7, 8]. The silver nanoparticles are other interesting metals with unique surface plasmon resonance (SPR) property that highly introduced them to the applications in biosensors and biomedical imaging. Silver has been used in ancient time as an effective antimicrobial agent in operations and utensils, and therefore has been widely introduced as antimicrobial and antifungal in industry. Recently, the silver nanoparticles

have been applied for cancer treatment causing selective induction of apoptosis [9, 10].

Current focus on core-shell metals has raised because their properties noticeably differ from their bulk. Metal core-shell nanoparticles demonstrated size-induced quantum-size confinement. A number of advanced functional applications as sensors, electronics, optoelectronics, and catalysis have been studied recently. Combining the properties of both kinds of NPs has interesting applications in surface-enhanced Raman scattering in catalytic degradation as electrochemical sensors or as inducers of apoptosis in cancer cells. Additionally, they have shown antibacterial and antifungal effects [9, 11].

We aim here to use the green facile one-pot route to synthesize an FeO@Ag core shell by allowing the growth of the magnetic nanoparticles in the medium containing the nucleation seeds of Ag atoms and the fungus filtrates to study the efficiency of three fungal species (*Aspergillus deflexus*, *Fusarium oxysporum*, and *Penicillium pinophilum*) in the production of the core shell functionalized with chitosan. The results revealed the formation of the nanocomposites by the help of the three species with the privilege of *F. oxysporum*. The data also show that the produced core-shell nanocomposites have minimum cytotoxicity, qualifying them for the applications in drug targeting vectors, cellular imaging, and hyperthermia.

## 2. Material and Methods

**2.1. Materials.** Iron (II) chloride-hexahydrate ( $\text{FeCl}_3 \cdot 6\text{H}_2\text{O}$ ) and ammonium iron (II) sulfate hexahydrate ( $(\text{NH}_4)_2\text{Fe}(\text{SO}_4)_2 \cdot 6\text{H}_2\text{O}$ ) were purchased from Merck (Germany) and used as received without any purification.

**2.2. Production of Biomass.** *Aspergillus deflexus*, *Penicillium pinophilum*, and *Fusarium oxysporum* were isolated from soil samples collected from local areas in Egypt (the three identified species were provided from Helwan University Faculty of Science, Department of Microbiology). Under shaking condition, fungal isolates were inoculated with potato dextrose flasks at 25°C [12].

**2.3. Identification of Isolates.** It was carried out at the genus level depending on their morphological characters as shown in the culture media (potato dextrose agar and Czapeks-dox agar media), also depending on the microscopic examination for conidia and hyphae [13–15]. The identification of fungal isolates was carried out in Mycology Lab of Botany and Microbiology Department, Faculty of Science, Helwan University.

**2.4. Intracellular Synthesis of Iron Oxide Nanoparticles.** Under aseptic conditions, the fungal filtrate has been separated from the mycelia. In a clean Erlenmeyer flask, the 5 mM  $\text{FeCl}_3$  and 2.5 mM  $\text{Fe}(\text{SO}_4)_2$  were mixed in 50 ml sterile distilled water and the pH adjusted to 12.5 under vigorous shaking for an hour at room temperature and therefore the formed seeds were separated. 2 mM  $\text{AgNO}_3$  has been added to 50 ml of the fungus filtrates. The magnetic nanoparticle seeds have been mixed with the later solution vigorous

shaking at 37°. After 72 hours, the nanoparticles have been separated by centrifugation at 10000 rpm at 0°C and washed several times. The formation of the core shell was examined by UV/visible and FTIR spectroscopy.

**2.5. Characterization of Nanoparticles.** A drop of the aqueous suspension of nanoparticles was placed on carbon-coated copper grids allowing the water to evaporate. The morphology and structure of samples were determined using HRTEM (JEM-2100HR, Japan) at 200 keV. XRD analyses were recorded on a Bruker D-8 powder X-ray diffractometer using  $\text{CuK}\alpha$  radiation ( $\lambda = 0.15418$  nm) over a  $2\theta$  range of 20°–90° with a step of 0.02. UV-visible absorption spectrophotometer (JASCO V-630), resolution 0.2 nm, is used to select the best species for the biosynthesis of core-shell nanoparticles and follow the formation of core-shell nanoparticles. Liquid samples were diluted at a 1 : 4 ratio and scanned in the range 200 to 800 nm. To study the molecular structure of the nanocomposite and the functional groups in the shell layer, Fourier transform infrared (FTIR) spectroscopy analysis was performed. The transmission-FTIR spectrum was acquired for the MID-Far range using diamond cell. The spectra were taken by a Vertex 70 Bruker Transform Infrared Spectrophotometer at a resolution of  $1\text{ cm}^{-1}$  in the range between 4000 and  $400\text{ cm}^{-1}$ . On the other hand, the ATR-FTIR measurements were taken by letting a drop of the suspended nanoparticles to evaporate on the surface of a germanium cell. Forty continuous cycles were acquired for each sample to ensure enough time for water molecule evaporation and efficient contact between the nanoparticles and the surface of the cell [12]. The particle size distribution and the zeta potential were determined by the dynamic light scattering (DLS) technique using a PSS-NICOMP 380-ZLS, USA. The measurement parameters were as follows: refractive index  $\text{RI} = 1.333$ ; viscosity = 0.933 cP; and room temperature. The magnetic properties of the nanoparticles have been examined using vibrating sample magnetometer (VSM), lake shore model 7410 (USA).

### 2.6. In Vitro Antitumor Bioassay on Human Tumor Cell Lines

**2.6.1. Cell Culture.** All cell lines were brought from ATCC via Vaccera tissue culture laboratories. All media were purchased from Lonza, Belgium, serum from Gibco, and trypsin and MTT from Bio Basic Canada. HepG2 cell line was maintained in RPMI-1640, MCF7, PC3, and HCT116 cell lines were maintained in DMEM high glucose with l-glutamine, 10% fetal bovine serum at 37°C in 5%  $\text{CO}_2$ , and 95% humidity. Cells were subcultured using trypsin, versene 0.15%.

**2.6.2. Viability Test.** After about 24 h of seeding  $10^4$  cells per well (in 96-well plates), cells have reached 60–70% confluence, the medium was changed to serum-free medium containing a final concentration of the test samples of 100 ppm in triplicates. The cells were treated for 72 h. 50  $\mu\text{M}$  of Doxorubicin was used as a positive control and serum-free medium was used as a negative control. Cell viability was determined using the MTT [3-(4,5-dimethylthiazol-2-yl)-2,5-diphenyltetrazolium bromide] assay as described by [16].

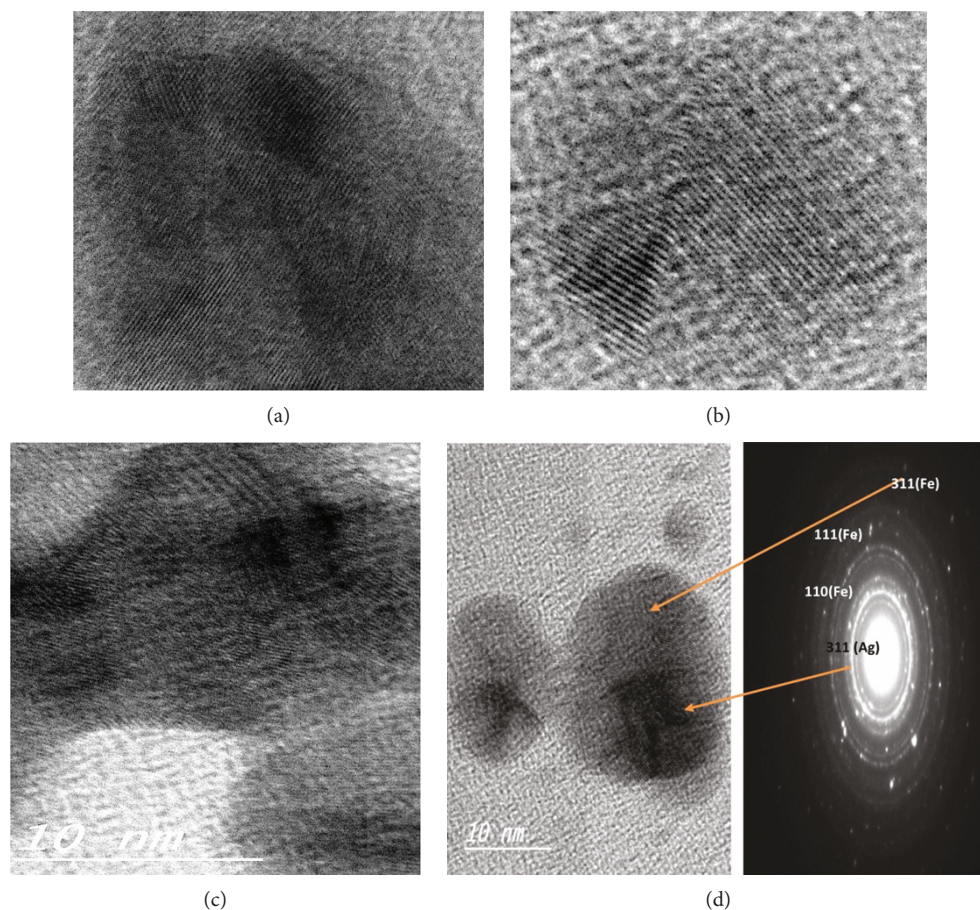
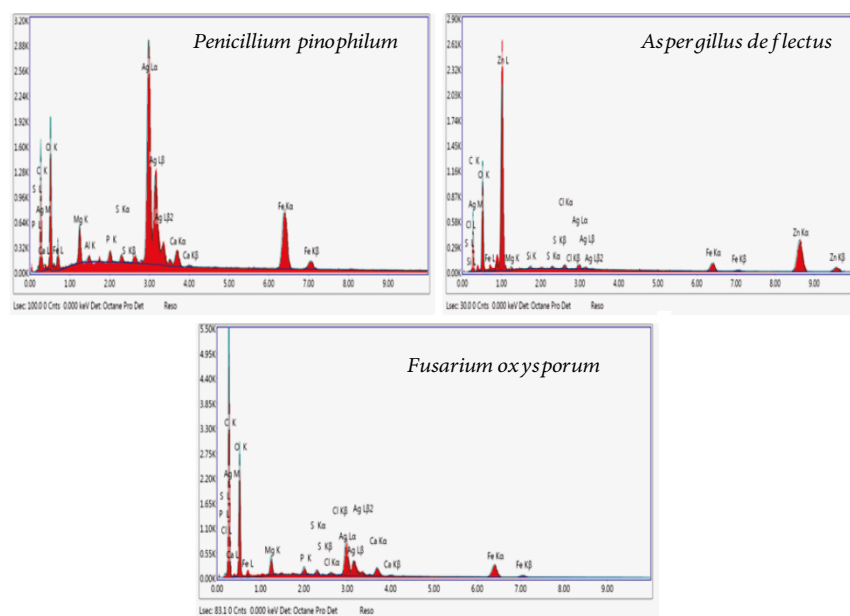


FIGURE 1: HRTEM of The Ag-FeO-Chitosan core shell NPs biosynthesized from (a) *A. deflectus*, (b) *F. oxysporum*, and (c) *P. pinophilium* and (d) the interplanar distance in the formed nanoparticles.

TABLE 1: The interplanar distances of the lattice fringes of Ag and  $\text{Fe}_3\text{O}_4$  phases and the particle sizes obtained from particle size distribution of HRTEM images and calculated from Debye-Scherrer equation.

Species	Lattice planes	Interplanar distances (HRTEM) (Å)	Interplanar distances (XRD) (Å)	Particle sizes (image J) (HRTEM) (nm)	Particle sizes (the Debye-Scherrer equation) (calculated) (nm)
<i>A. deflectus</i>	311(Fe)	2.5			
	111	2.3	2.35		
	200	2.0	2.08	$7.29 \pm 3.8$	$7.115 \pm 0.79$
	220	1.6	1.44		
<i>P. pinophilium</i>	311 (Ag)		1.23		
	311(Fe)	2.7	2.52		
	111	2.4	2.36		
	200	2.0	2.04	$6.01 \pm 2.6$	$9.65 \pm 1.35$
	220		1.44		
	311 (Ag)		1.23		
<i>F. oxysporum</i>	311(Fe)	2.4	2.54		
	111	2.33	2.36		
	200	2.05	2.05	$5.72 \pm 1.7$	$9.25 \pm 1.54$
	220	1.96	1.44		
	311 (Ag)		1.23		



Elements	Weight %		
	<i>P. pinophilum</i>	<i>A. delectus</i>	<i>F. oxysporium</i>
C K	13.23	16.68	24.38
AgL	23.57	0.87	3.41
FeK	12.77	2.39	2.38
Oxygen	47.27	52.81	67.91

FIGURE 2: EDAX of FeO@Ag@chitosan core shell biosynthesized from the three species: *P. pinophilum*, *A. delectus*, and *F. oxysporium*. The attached table summarizes the %weight of the elements in the core-shell nanocomposite from each species.

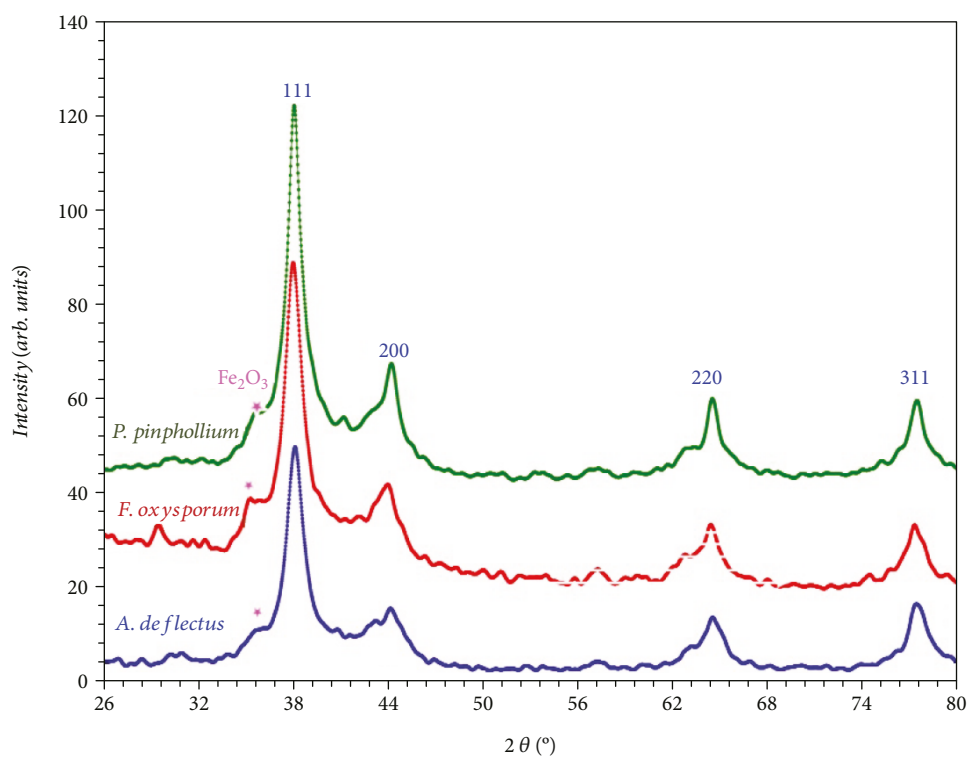


FIGURE 3: XRD of  $\gamma\text{Fe}_2\text{O}_3$ @Ag functionalized with chitosan core shell biosynthesized from the three species: green: *P. pinophilum*, red: *F. oxysporum*, and blue: *A. delectus*.

The equation used for calculation of percentage cytotoxicity:  $(1 - ((x)/(Av(NC)))) * 100$ , where Av is the average, X is the absorbance of sample well measured at 595 nm with reference 690 nm, and NC is the absorbance of negative control measured at 595 nm with reference 690 nm.

### 3. Results and Discussion

**3.1. Core-Shell Structure of  $\gamma\text{Fe}_2\text{O}_3@Ag@Chitosan$  NPs.** The bright-field TEM and high-resolution TEM (HRTEM) can be used to discern different compositions based on lattice fringes and contrast variations. The high-resolution transmission electron microscope (HRTEM) in Figures 1(a)–1(d) shows the formation of spherical polycrystalline core-shell nanoparticles with the Ag (dark) surrounded by the FeO (lighter) in agreement to the Z-contrast theory [17]. This arrangement can be understood in view of experimental procedures in which we have allowed the AgNp seeds to grow in the presence of the fungal filtrates for 72 hrs, whereas the FeO seeds were separated from the precursor pot immediately after precipitation and therefore added to the pot containing the  $\text{AgNO}_3$  and the filtrate which contains the chitosan as a main component of the fungal cell wall and which is responsible for the capping and the control of nanoparticle sizes [8, 18]. The average sizes measured using the particle analysis of image J are  $6.01 \pm 2.6$ ,  $5.7 \pm 1.07$ , and  $7.29 \pm 3.8$ , compared to that calculated from the Debye-Scherrer equation were  $9.65 \pm 1.35$ ,  $9.25 \pm 1.54$ , and  $7.115 \pm 0.79$  nm for *Penicillium*, *Fusarium*, and *Aspergillus*, respectively. The highly magnified HRTEM shows that the lattice interplanar distances vary according to the diffraction phases. Figures 1(a)–1(c) show the formation of the core shell in the *A. deflectus*, *F. oxysporum*, and *P. pinophilum*, respectively, whereas Figure 1(d) shows the selected area electron diffraction (SAED) interplanar fringe distances and their corresponding in the formed nanoparticles. All analysis has been performed using image J program.

Table 1 summarizes the interplanar distances of the lattice fringes of Ag and FeO phases synthesized using the three species. The table compares between the d-spacing obtained from the XRD data and that observed from the HRTEM pictures and measured using the image J program.

The measured interplanar distances are comparable to the data obtained from XRD corresponding to each phase which confirm the formation of Ag-FeO-based core-shell nanoparticles from the three species. The particle sizes measured from HRTEM pictures using image J are also comparable to that calculated from the Debye-Scherrer equation. Collective data confirm that the particle size of the  $\text{FeO}@Ag@chitosan$  core-shell NPs is  $<10$  nm.

The EDAX data in Figure 2 reveals the presence of the Ag, Fe, and O peaks in different ratios for the three samples; although the preparation procedure is the same, this could be due to the selective differences of metal bioremediation by fungal species.

XRD patterns (Figure 3) demonstrate the high crystallinity of the two phases: Ag and  $\gamma\text{Fe}_2\text{O}_3$ . The diffraction peak positions match with the face-centered cubic structure of Ag and  $\gamma\text{Fe}_2\text{O}_3$ . The diffraction peak (311) plane corresponds

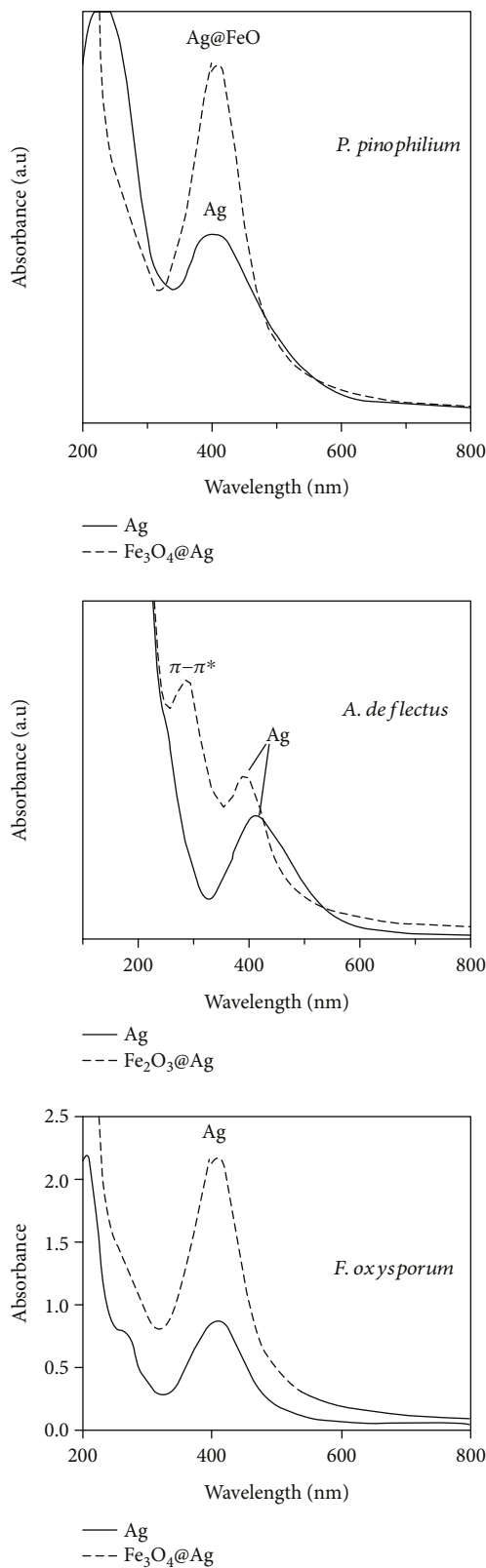


FIGURE 4: The surface plasmon resonance (SPR) of Ag (previous work) and  $\gamma\text{Fe}_2\text{O}_3@Ag$  functionalized with chitosan core shell biosynthesized from the three species: *P. pinophilum*, *A. deflectus*, and *F. oxysporum*.

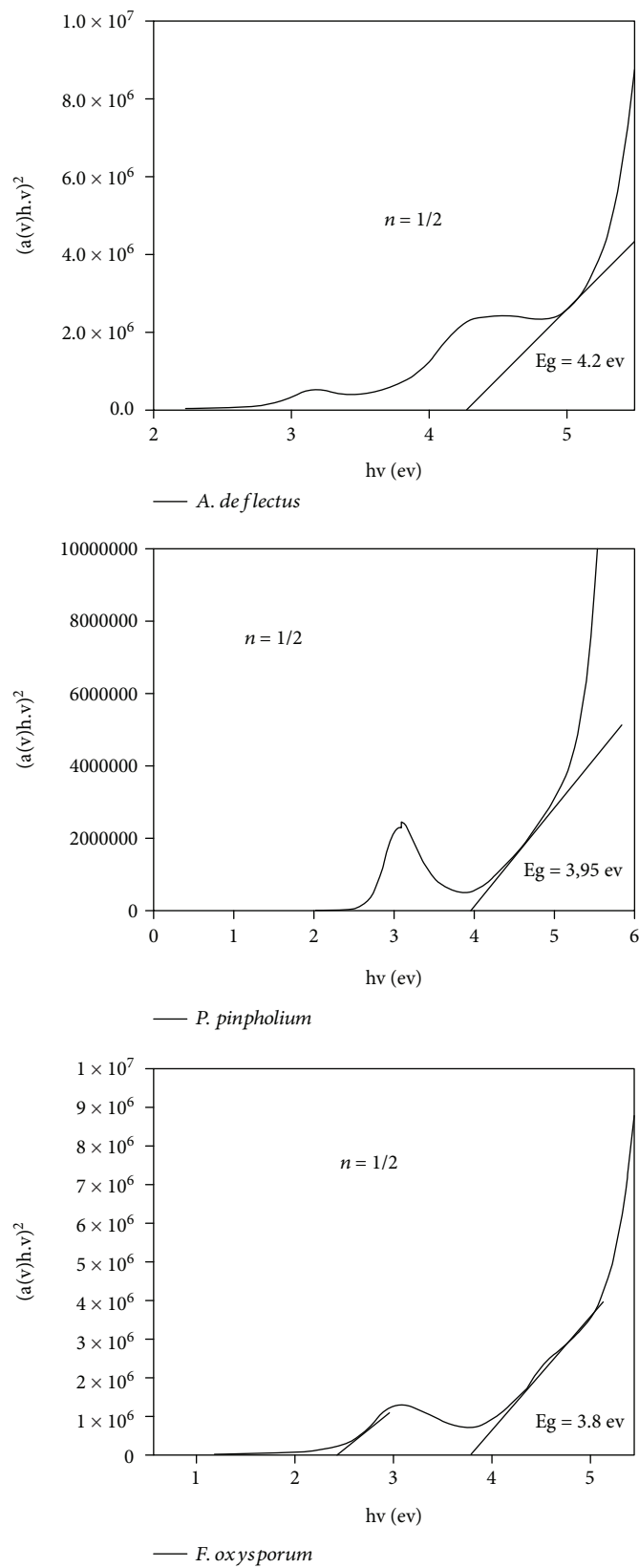


FIGURE 5: The energy band gap calculated from the Beer-Lambert's law and the best fit was with  $n = 1/2$  (allowed transition) value for  $\gamma\text{Fe}_2\text{O}_3@Ag$  functionalized with chitosan core shell biosynthesized from the three species: *P. pinophilum*, *A. deflectus*, and *F. oxysporum*.

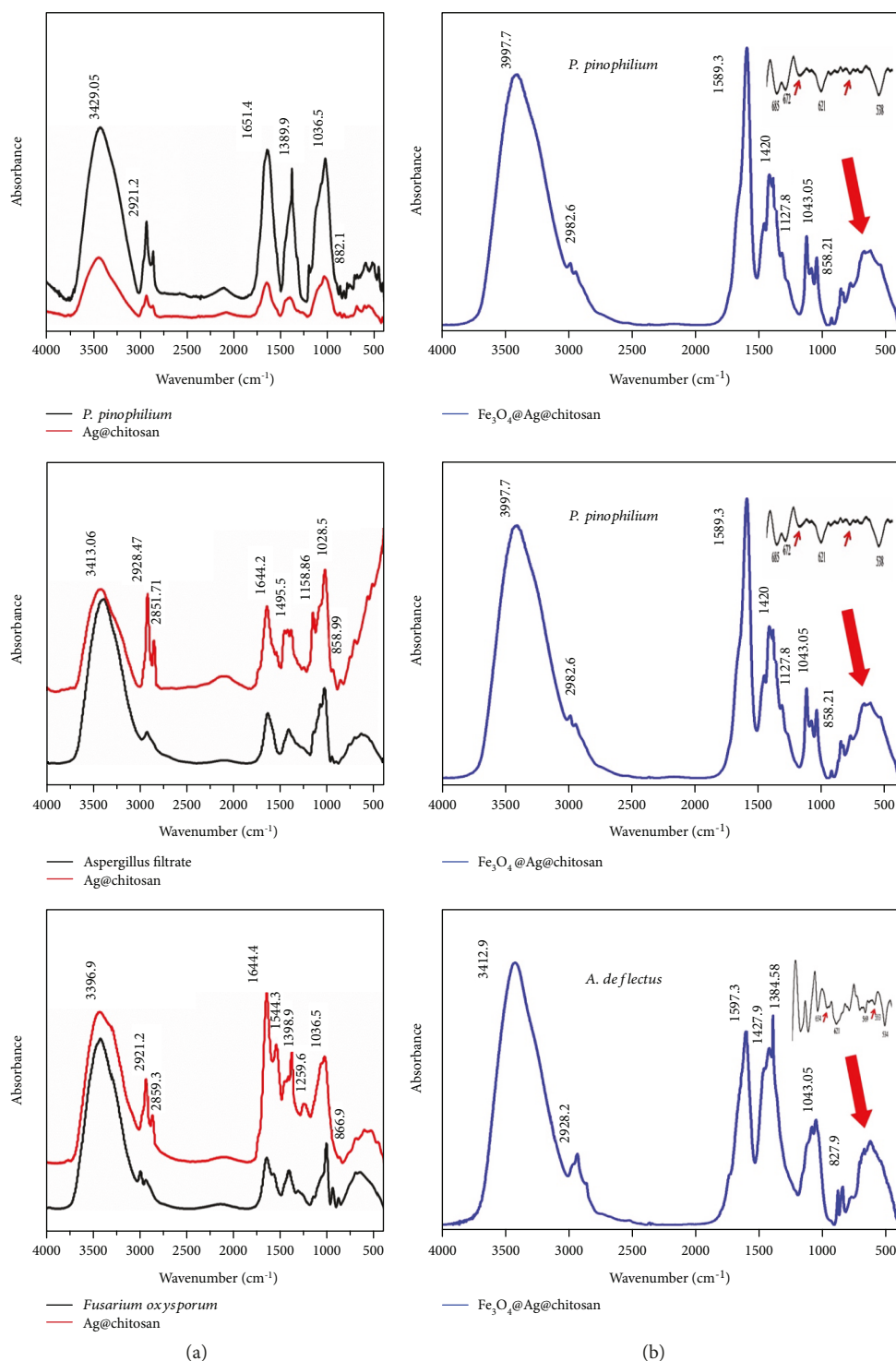


FIGURE 6: The transmission FTIR spectrum showing the molecular structure of the  $\gamma\text{Fe}_2\text{O}_3$ @Ag@chitosan biosynthesized of *P. pinophilum*, *A. deflectus*, and *F. oxysporum* compared to Ag@chitosan (a), the ATR-IR spectrum of the molecular structure of the surface layer of the core shell (b) showing the second derivatives for the region 700–500 cm<sup>-1</sup>.

to the maghemite, with  $2\theta$  value 35.7, whereas the diffraction peak positions (111), (200), (220), and (311) at  $2\theta$ ; 38.1, 44, 64, and 77.4, respectively, are attributed to the presence of Ag face-centered cubic structure. These peak positions confirm the formation of maghemite  $\gamma\text{Fe}_2\text{O}_3$ @Ag phases and

lattice interspacing values are in agreement with the work of Cui et al. [19]. We used the Debye-Scherrer formula to estimate the particle NP sizes:  $D = 0.9\lambda/\beta \cos\theta$ , where  $\lambda$  is the wavelength of the X-ray (0.1541 nm),  $\beta$  is FWHM (full width at half maximum),  $\theta$  is the diffraction angle and  $D$  is the

TABLE 2: The particles sizes distribution, polydispersity indices, and the zeta potential data of  $\gamma\text{Fe}_2\text{O}_3@Ag$  biosynthesized from *A. defluctus*, *F. oxysporum*, and *P. pinophilium*.

	Size (nm)	PDI	Zeta potential
<i>A. defluctus</i>	826	0.325	-4.81
<i>F. oxysporum</i>	718.9	0.434	-9.33
<i>P. pinophilium</i>	632.0	0.239	-6.75

particle diameter size in nm, Bragg slow:  $2d \sin \theta = n \lambda$  has used for the  $d$  (interplanar spacing between atoms) and the calculated values were as shown in Table 1.

**3.2. Spectroscopic Characterization of  $\gamma\text{Fe}_2\text{O}_3@Ag@Chitosan$  Core-Shell NPs.** The process of synthesis takes place by a novel and easy one-pot green method using the filtrates of three fungal species; *P. pinophilium*, *A. defluctus*, and *F. oxysporum*. The  $Ag^+$  were allowed to reduce into atom seeds in the presence of fungal filtrates, followed by the growing of maghemite NP layers on the top of the Ag core at the same pot at room temperature. The metabolites and chitin (the main constituent of the fungal cell wall) were the reducing agents of Ag atoms into Ag ions and later on, played the capping role to control the size of the core shell in the reaction.

The contribution of polysaccharide extracted from the fungus in the reduction of silver ions to silver atoms has been examined by UV/vis (data not shown). UV/visible absorption has been employed to analyze the surface plasmon resonance (SPR) of pure AgNP and core-shell  $\gamma\text{Fe}_2\text{O}_3@Ag$  [20]. In a previous work, we have assigned the SPR for Ag (Figure 4) at 403, 417, and 410 nm for *P. pinophilium*, *A. defluctus*, and *F. oxysporum*, respectively [13–15, 21]. UV/visible spectrum of  $\gamma\text{Fe}_2\text{O}_3@Ag$  nanocomposite (Figure 4) shows a blue shift of SPR to 394 nm and 407 nm for *A. defluctus* and *F. oxysporum*, respectively, whereas no change occurs for that synthesized from *P. pinophilium*. As the particle size decreases, the band gap of a material increases which results in the shifting of the absorption peak to the lower wavelength [22]. The data show enhancement of the SPR peak intensity of  $\gamma\text{Fe}_2\text{O}_3@Ag$  comparing to the corresponding Ag. It has been proved that the magnetic nanoparticles have a high refractive index that enables them to improve effectively the SPR [7, 23].

The optical band gap has been calculated from the absorption coefficient data as a function of wavelength by using the Tauc relation equation:  $\alpha h\nu = \beta(h\nu - E_p)^n$  where  $\alpha$  is the absorption coefficient,  $h\nu$  is the photon energy in eV,  $\beta$  is a band-tailing parameter,  $E_p$  is the optical band gap of the nanoparticle, and  $n = 0.5$  for a direct band gap and  $n = 2$  for an indirect transition.

The data shows (Figure 5) that the energy band gaps for the core-shell  $\gamma\text{Fe}_2\text{O}_3@Ag$  are 3.9, 4.2, and 3.8 eV for *P. pinophilium*, *A. defluctus*, and *F. oxysporum*, respectively. The data reveals that the  $E_g$  for the core shell increases comparing to the value of  $E_g$  for Ag that has been recorded in previous work at 2.3 and 2.23 eV for *P. pinophilium* and *A. defluctus*, respectively, at the same pH. The increase in the energy band

gap is in agreement with the blue shift in the Ag SPR in the core-shell nanoparticles and can be attributed to the decrease in the crystallite size due to the confinement effect [24].

The transmission FTIR spectrum (Figures 6(a)) examined the vibrational bands in the nanocomposite and therefore, the formation of the  $\gamma\text{Fe}_2\text{O}_3@Ag$  functionalized with chitosan. The absorption band at  $684\text{ cm}^{-1}$  is attributed in other works to the vibrations of the Fe–O bond, and therefore used to confirm the formation of iron oxide nanoparticles [25–27]. The FTIR results (Figure 6) show the Fe–O bond at  $621\text{ cm}^{-1}$  for the three pieces. The blue shift of the Fe–O band from  $684$  to  $621\text{ cm}^{-1}$  may be attributed to the bonding between chitosan and iron oxide group [8]. This band confirms the formation of the  $\gamma\text{Fe}_2\text{O}_3$  according to the work previously shown by Xin Zhang at 2003. According to Du et al., the complexity of the unit cell of maghemite comparing to maghemite causes the formation of more Raman- and infrared-active phonons. [28, 29].

The ATR-FTIR spectrum (Figures 6(b)) shows two bands of exopolysaccharides at  $1654.80\text{ cm}^{-1}$  assigned to C–O stretching vibration of an *N*-acetyl group and at  $1596.94\text{ cm}^{-1}$  due to an N–H stretching of a primary amine group characteristic bands. The strong absorption at  $1038\text{ cm}^{-1}$  assigned to C–O–C stretching vibrations indicates that the monosaccharide in EPS has a pyran structure. We have assigned these bands in previous work [13–15] for chitosan, in addition to the absorption band at  $877\text{ cm}^{-1}$  (C–N finger-print band of chitosan) suggesting that the glucoside bond in the exopolysaccharides is  $\beta$ -linkage ([8]). The C–O–C peak exhibits red shift into  $1043\text{ cm}^{-1}$  for the three species, whereas the C–N fingerprint of chitosan assigned before at  $877\text{ cm}^{-1}$  [13–15] exhibits blue shift into  $835.1$ ,  $827.9$ , and  $858.2\text{ cm}^{-1}$  for *F. oxysporum*, *A. defluctus*, and *P. pinophilium*, respectively. The blue shift could be attributed to the interaction of chitosan with the Ag/maghemite core-shell surface via its C–N groups [22]. The weak band at  $1743\text{ cm}^{-1}$  that appears in the *Fusarium* spectrum has been attributed to the presence of C=O vibration confirming that some of the chitosan polymeric chains have been opened upon adsorption on the maghemite nanoparticles [22]. The second derivative of the region  $700\text{--}500\text{ cm}^{-1}$  showed bands at  $621$ , and  $538\text{ cm}^{-1}$  for *P. Pinophilium*,  $621$ , and  $528\text{ cm}^{-1}$  for *A. defluctus*, and  $638$ , and  $575\text{ cm}^{-1}$  for *F. oxysporum*. These bands have been assigned for the  $\gamma\text{Fe}_2\text{O}_3$  iron oxide phase [29]. The FTIR data is in agreement with the work done by López et al. and Liang et al. [10, 30] interpreting the same peaks for the formation of chitosan coating layer around the core shell.

**3.3. Validation of the Application of  $\gamma\text{Fe}_2\text{O}_3@Ag@Chitosan$  Core-Shell NPs.** Table 2 show the Dynamic light scattering results obtained for the particle size distribution (nm), Poly-dispersity indices, and zeta potential of the  $\gamma\text{Fe}_2\text{O}_3@Ag@chitosan$  core-shell NPs biosynthesized from *P. pinophilium*, *A. defluctus*, and *F. oxysporum*.

The DLS data (Table 2) show that the Polydispersity indices of the bio-synthesized nanoparticles are less than 0.7 indicating that their sizes were homogeneously distributed. The particle size distribution is relatively high

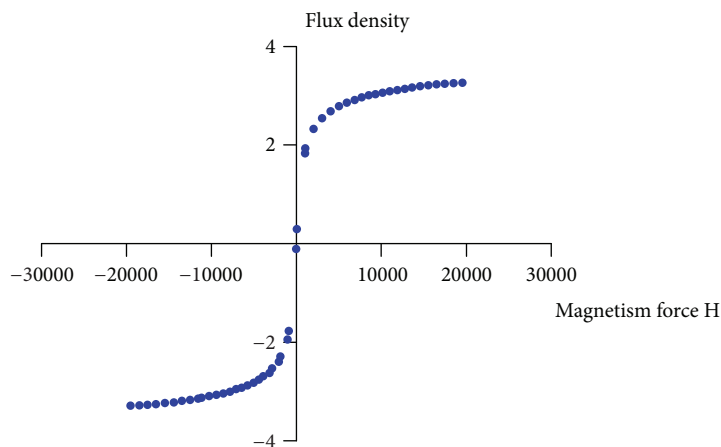


FIGURE 7: The magnetic hysteresis curve of the  $\gamma\text{Fe}_2\text{O}_3@Ag$  functionalized with chitosan core-shell biosynthesized from *F. oxysporum*.

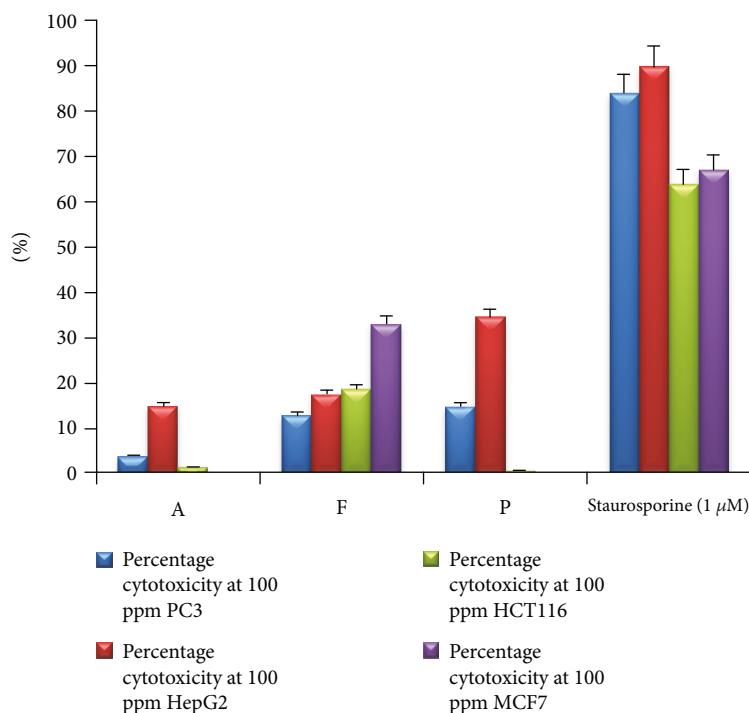


FIGURE 8: The cytotoxicity effect of 100 ppm  $\gamma\text{Fe}_2\text{O}_3@Ag$  from *A. deflectus* (A), *F. oxysporum* (F), and *P. pinophilum* (P) on human prostatic adenocarcinoma (PC3), human liver hepatocellular carcinoma (HepG2), human colorectal carcinoma (HCT116), and human breast adenocarcinoma (MCF7) cell lines.

comparing to the data obtained from the HRTEM, this can be due to that the DLS take into account the size of the charge cloud surrounding the particles, or it could be due to the agglomeration of the particles. As the value of zeta potential determines the degree of repulsion between particles, therefore, the more this value is away from zero the less the flocculating of these particles. In zeta potential value evaluation pH should be considered, as the solution is more alkaline, the tendency of the negativity of the particles increases. The zeta potential results indicate that the particles are arranged as following considering the dispersity: *Fusarium* > *deflectus* > *pinophilum*. The

negativity of the particles is confirming that the pH of the solution was alkaline.

Figure 7 shows the magnetic hysteresis curve of the  $\gamma\text{Fe}_2\text{O}_3@Ag$  nanoparticles. The M-H curve shows no hysteresis, and the forward and backward magnetization curves overlap completely and are almost negligible, moreover, the coercivity is nearly zero confirming the formation of super para-magnetic nanoparticles. These results are in agreement with the work of López et al. and Gregorio-Jauregui et al. [10, 18].

Three core-shell nanoformulas have been studied for four cancer cell lines, prostate, liver, colon, and breast using the

TABLE 3: The cytotoxic effect of the samples at 100 ppm on human prostatic adenocarcinoma (PC3), human liver hepatocellular carcinoma (HepG2), human colorectal carcinoma (HCT116), and human breast adenocarcinoma (MCF7) cell lines.

	Percentage cytotoxicity at 100 ppm			
	PC3	HepG2	HCT116	MCF7
<i>A. deflectus</i>	4%	15%	1.5%	0%
<i>P. pinophilium</i>	15%	34.7%	0.7%	0%
<i>F. oxysporum</i>	13%	17.7%	18.8%	33.2%
Staurosporine (1 $\mu$ M)	84%	90%	64%	67%

MTT assay. The data showed that the formula is safe on human studied tumor cells up to 10,100 ppm, which could be an indication of its safety on normal human somatic cells as well. The safest formula was *A. deflectus* as it was inactive against all four cell lines under examination. Formula *F. oxysporum* had a weak cytotoxic effect on MCF7 while *P. pinophilium* had a weak cytotoxic effect on HepG2 (Figure 8 and Table 3) [13–15, 31–33].

#### 4. Conclusion

To sum up, we have established a one-pot, easy, and clean green protocol to synthesize monodispersed, crystalline, superparamagnetic  $\gamma$ -Fe<sub>2</sub>O<sub>3</sub>-based Ag coated with chitosan core shell at room temperature. The results confirm the magnetic and plasmonic properties of the composite. Results confirmed that the three species were efficient in the biosynthesis of the core-shell nanocomposites but the *Fusarium oxysporum* shows lowest particle size distribution and best zeta potential. The cytotoxicity of the core shell from the three species was very low (less than 20%) on all the studied cell lines but that of *F. oxysporum* shows 30% cytotoxicity with MCF7 and *P. pinophilium* shows 33% with PC3 at the 100 ppm dose. These results suggest that these nanoparticles are safe as drug carriers, imaging, and hyperthermia. The novelty in this work is the facile route of nano core-shell synthesis and the potential employment in medical application. The formation of the core-shell  $\gamma$ -Fe<sub>2</sub>O<sub>3</sub>-based Ag functionalized with chitosan has opened for us multiple chances for the synthesis of several kinds of core-shell nanoparticles that could be safely used in drug delivery, biosensing, and imaging.

Conclusive characterization data confirm the formation of  $\gamma$ -Fe<sub>2</sub>O<sub>3</sub>-based Ag coated with chitosan core shell using a one-pot biosynthesis method. The particle size, shape, super paramagnetic properties, zeta potential data, and low cytotoxicity set them up as a perfect candidate for the drug and gene delivery, biosensors, and hyperthermia [34–36]. This work was a part of a project to select the perfect fungal species for the biosynthesis of the plasmonic@superparamagnetic core-shell nanoparticles. This work has been completed by the selection of the *Fusarium oxysporum*. The other part of the work (has been already published [12] has studied the optimized conditions for the preparation of a biocompatible with suitable physico-chemical properties NPs.

#### Data Availability

The data used to support the findings of this study are available from the corresponding author upon request.

#### Conflicts of Interest

The authors declare that they have no conflicts of interest.

#### Acknowledgments

We appreciate the kind providing of the identified species from Helwan University Faculty of Science, Department of Microbiology. This study was funded by the Science and Technology Development Fund in Egypt (12649).

#### References

- [1] R. P. Feynman, "There's plenty of room at the bottom," *Engineering and Science*, vol. 23, no. 5, pp. 22–36, 1960.
- [2] N. Taniguchi, "On the basic concept of nanotechnology," in *Proceedings of the International Conference on Production Engineering, Part II, Japan Society of Precision Engineering*, pp. 18–23, Tokyo, Japan, February 1974.
- [3] P. Mulvaney, "Nanoscience vs nanotechnology—defining the field," *ACS Nano*, vol. 9, no. 3, pp. 2215–2217, 2015.
- [4] A. Atta, G. el-Mahdy, H. al-Lohedan, and S. al-Hussain, "Synthesis of environmentally friendly highly dispersed magnetite nanoparticles based on rosin cationic surfactants as thin film coatings of steel," *International Journal of Molecular Sciences*, vol. 15, no. 4, pp. 6974–6989, 2014.
- [5] S. Irvani, "Green synthesis of metal nanoparticles using plants," *Green Chemistry*, vol. 13, no. 10, pp. 2638–2650, 2011.
- [6] V. V. Makarov, A. J. Love, O. V. Sinityna et al., "Green nanotechnologies: synthesis of metal nanoparticles using plants," *Acta Naturae*, vol. 6, 2014.
- [7] R. P. Liang, G. H. Yao, L. X. Fan, and J. D. Qiu, "Magnetic Fe<sub>3</sub>O<sub>4</sub>@Au composite-enhanced surface plasmon resonance for ultrasensitive detection of magnetic nanoparticle-enriched  $\alpha$ -fetoprotein," *Analytica Chimica Acta*, vol. 737, pp. 22–28, 2012.
- [8] Z. Marková, K. Šišková, J. Filip et al., "Chitosan-based synthesis of magnetically-driven nanocomposites with biogenic magnetite core, controlled silver size, and high antimicrobial activity," *Green Chemistry*, vol. 14, no. 9, pp. 2550–2558, 2012.
- [9] M. E. F. Brollo, R. López-Ruiz, D. Muraca, S. J. A. Figueroa, K. R. Pirota, and M. Knobel, "Compact Ag@Fe<sub>3</sub>O<sub>4</sub> core-shell nanoparticles by means of single-step thermal decomposition reaction," *Scientific Reports*, vol. 4, no. 1, p. 6839, 2014.
- [10] R. López, M. Pineda, G. Hurtado et al., "Chitosan-coated magnetic nanoparticles prepared in one step by reverse microemulsion precipitation," *International Journal of Molecular Sciences*, vol. 14, no. 10, pp. 19636–19650, 2013.
- [11] K. S. Kumar, V. B. Kumar, and P. Paik, "Recent advancement in functional core-shell nanoparticles of polymers: synthesis, physical properties, and applications in medical biotechnology," *Journal of Nanoparticles*, vol. 2013, Article ID 672059, 24 pages, 2013.
- [12] M. M. Eid, S. M. El-Hallouty, M. El-Manawaty, F. H. Abdelzaher, M. Al-Hada, and A. M. Ismail, "Preparation conditions effect on the physico-chemical properties of

- magnetic-plasmonic core-shell nanoparticles functionalized with chitosan: green route," *Nano-Structures & Nano-Objects*, vol. 16, pp. 215–223, 2018.
- [13] M. E. Osman, M. M. Eid, O. k. H. Khattab, S. M. el-Hallouty, S. M. el-Marakby, and D. A. Mahmoud, "Spectroscopic characterization of the effect of gamma radiation on the physical parameters of biosynthesized silver/chitosan nano-particles and their antimicrobial activity," *Materials Research Express*, vol. 2, no. 9, article 095023, 2015.
- [14] M. E. Osman, M. M. Eid, O. H. Khattab, S. M. Abd-El All, S. M. El-Hallouty, and D. A. Mahmoud, "Optimization and spectroscopic characterization of the biosynthesized silver/chitosan nanocomposite from aspergillus deflectus and Penicillium pinophilum," *Journal of Chemical, Biological and Physical Sciences*, vol. 5, no. 3, p. 2643, 2015.
- [15] M. E. Osman, M. M. Eid, O. H. Khattab, S. M. El-Hallouty, M. El-Manawaty, and A. D. Mahmoud, "In vitro cytotoxicity of biosynthesized Ag/CS NP against MCF7, PC3 and A549 Cancer cell lines," *International Journal of PharmTech Research*, vol. 8, no. 5, pp. 1011–1017, 2015.
- [16] T. Mosmann, "Rapid colorimetric assay for cellular growth and survival: application to proliferation and cytotoxicity assays," *Journal of Immunological Methods*, vol. 65, no. 1-2, pp. 55–63, 1983.
- [17] B. R. Knappett, P. Abdulkin, E. Ringe et al., "Characterisation of Co@Fe<sub>3</sub>O<sub>4</sub> core@shell nanoparticles using advanced electron microscopy," *Nanoscale*, vol. 5, no. 13, pp. 5765–5772, 2013.
- [18] K. M. Gregorio-Jauregui, M. G. Pineda, J. E. Rivera-Salinas et al., "One-step method for preparation of magnetic nanoparticles coated with chitosan," *Journal of Nanomaterials*, vol. 2012, Article ID 813958, 8 pages, 2012.
- [19] H. Cui, Y. Liu, and W. Ren, "Structure switch between  $\alpha$ -Fe<sub>2</sub>O<sub>3</sub>,  $\gamma$ -Fe<sub>2</sub>O<sub>3</sub> and Fe<sub>3</sub>O<sub>4</sub> during the large scale and low temperature sol-gel synthesis of nearly monodispersed iron oxide nanoparticles," *Advanced Powder Technology*, vol. 24, no. 1, pp. 93–97, 2013.
- [20] M. M. Rahman, A. M. Aisiri, A. Jamal, M. Faisal, and S. B. Khan, *Iron Oxide Nanoparticles*, INTECH Open Access Publisher, 2011.
- [21] M. E. Osman, M. M. Eid, O. H. Khattab, S. M. El-Hallouty, and D. A. Mahmoud, "Biosynthesis of silver nano-particles by local fungal isolates from Egyptian soil," *Quantum Matter*, vol. 5, no. 2, pp. 305–311, 2016.
- [22] K. Shameli, M. M. B. Ahmad, W. Z. Yunis et al., "Synthesis and characterization of silver/montmorillonite/chitosan bionanocomposites by chemical reduction method and their antibacterial activity," *International Journal of Nanomedicine*, vol. 6, pp. 271–284, 2011.
- [23] D. M. Fouad, W. A. El-Said, and M. B. Mohamed, "Spectroscopic characterization of magnetic Fe<sub>3</sub>O<sub>4</sub>@Au core shell nanoparticles," *Spectrochimica Acta Part A: Molecular and Biomolecular Spectroscopy*, vol. 140, pp. 392–397, 2015.
- [24] M. Stefan, O. Pana, C. Leostean et al., "Synthesis and characterization of Fe<sub>3</sub>O<sub>4</sub>-TiO<sub>2</sub> core-shell nanoparticles," *Journal of Applied Physics*, vol. 116, no. 11, article 114312, 2014.
- [25] P. E. G. Casillas, C. A. M. Pérez, and C. A. R. Gonzalez, "Infrared spectroscopy of functionalized magnetic nanoparticles," in *Infrared Spectroscopy - Materials Science, Engineering and Technology*, pp. 405–420, INTECH Open Access Publisher, 2012.
- [26] V. Sureshkumar, S. C. G. Kiruba Daniel, K. Ruckmani, and M. Sivakumar, "Fabrication of chitosan-magnetite nanocomposite strip for chromium removal," *Applied Nanoscience*, vol. 6, no. 2, pp. 277–285, 2016.
- [27] R. D. Waldron, "Infrared spectra of ferrites," *Physical Review*, vol. 99, no. 6, pp. 1727–1735, 1955.
- [28] N. Du, Y. Xu, H. Zhang, C. Zhai, and D. Yang, "Selective synthesis of Fe<sub>2</sub>O<sub>3</sub> and Fe<sub>3</sub>O<sub>4</sub> nanowires via a single precursor: a general method for metal oxide nanowires," *Nanoscale Research Letters*, vol. 5, no. 8, pp. 1295–1300, 2010.
- [29] X. Zhang, Y. Niu, X. Meng, Y. Li, and J. Zhao, "Structural evolution and characteristics of the phase transformations between  $\alpha$ -Fe<sub>2</sub>O<sub>3</sub>, Fe<sub>3</sub>O<sub>4</sub> and  $\gamma$ -Fe<sub>2</sub>O<sub>3</sub> nanoparticles under reducing and oxidizing atmospheres," *CrystEngComm*, vol. 15, no. 40, p. 8166, 2013.
- [30] W. I. Liang, X. Zhang, Y. Zan et al., "In situ study of Fe<sub>3</sub>Pt-Fe<sub>2</sub>O<sub>3</sub> core-shell nanoparticle formation," *Journal of the American Chemical Society*, vol. 137, no. 47, pp. 14850–14853, 2015.
- [31] S. M. Bassef, W. Fayad, M. Khaled et al., "Antiproliferation effects of Sophora japonica," *Indian Journal of Experimental Biology*, vol. 48, pp. 258–264, 2010.
- [32] M. El Manawaty, W. A. Fayad, N. M. El-Fiky, G. M. Wassel, and B. S. EL-Menshawi, "High-throughput screening of 75 euphorbiaceae and myrtaceae plant extracts for in-vitro anti-tumor and pro-apoptotic activities on human tumor cell lines, and lethality to brine shrimp. Internat.," *Journal of Pharmacy and Pharmaceutical Sciences*, vol. 5, pp. 178–183, 2013.
- [33] B. S. El-Menshawi, W. Fayad, K. Mahmoud et al., *Screening of Natural Products for Therapeutic Activity against Solid Tumors*, CSIR, 2010.
- [34] H. El Ghandoor, H. M. Zidan, M. M. Khalil, and M. I. Ismail, "Synthesis and some physical properties of magnetite (Fe<sub>3</sub>O<sub>4</sub>) nanoparticles," *International Journal of Electrochemical Science*, vol. 7, no. 6, pp. 5734–5745, 2012.
- [35] B. Issa, I. Obaidat, B. Albiss, and Y. Haik, "Magnetic nanoparticles: surface effects and properties related to biomedicine applications," *International Journal of Molecular Sciences*, vol. 14, no. 11, pp. 21266–21305, 2013.
- [36] S. A. Kulkarni, P. S. Sawadh, and P. K. Palei, "Synthesis and characterization of superparamagnetic Fe<sub>3</sub>O<sub>4</sub>@SiO<sub>2</sub> nanoparticles," *Journal of the Korean Chemical Society*, vol. 58, no. 1, pp. 100–104, 2014.



**Hindawi**  
Submit your manuscripts at  
[www.hindawi.com](http://www.hindawi.com)

